EEET ECOLOGICAL ENGINEERING & ENVIRONMENTAL TECHNOLOGY

Ecological Engineering & Environmental Technology, 2026, 27(9), 110–131
https://doi.org/10.12912/27197050/226093
ISSN 2719–7050, License CC-BY 4.0

Received: 2026.07.14
Accepted: 2026.08.03
Published: 2026.08.15

Forty years of Landsat and Sentinel-2 retrospective analysis reveal a species-differentiated dieback signal in the Atlas forests of Béni Mellal-Khénifra (Morocco)

Yacine Laidi[1*], Nawfel El Bouchti[2], Younes Abbas[1], Khalid Benhssaine[2], Mohamed El Mderssa[1]

[1] Faculty of Applied Sciences of Beni Mellal, Sultan Moulay Slimane University Beni Mellal, BP592, 23000, Beni Mellal, Morocco
[2] National Agency of Waters and Forests, Morocco
* Corresponding author's e-mail: yacinlaidi91@gmail.com

ABSTRACT

Long-term, spatially explicit reconstructions of forest dieback are scarce for the southern African rim of the Mediterranean basin. This study presents an open, reproducible retrospective analysis of natural forest dieback in the Béni Mellal-Khénifra region of Morocco (936,437 ha) over 1984–2024. Six strata of the Second National Forest Inventory dominated by *Cedrus atlantica*, *Quercus rotundifolia* and *Quercus suber* were sampled through a stratified random design (2.901 Landsat pixels; 2.933 Sentinel-2 pixels). Per-pixel NDVI series were processed with a BFAST-like workflow combining STL decomposition and PELT change-point detection, and complemented by a recent-decline detector to rescue near-edge signals. Species-level NDVI anomalies were cross-correlated with SPEI at 3-, 6- and 12-month scales and with vapour-pressure-deficit anomalies, with autocorrelation-corrected significance testing. A cumulated dieback signal of approximately 187,700 ha (20.1% of the regional forest cover; bootstrap 95% CI 155,500–221,600 ha) was identified. Cork oak showed the highest relative rate (41.4% of pure stands) and holm oak the largest absolute affected area (142,591 ha). SPEI-12 emerged as the strongest hydroclimatic correlate, particularly for cork oak ($r = +0.364$ at lag 0), while VPD anomalies co-varied with concurrent NDVI depressions in all three species. Sentinel-2 detected +18.3 to +26.3 percentage points more Atlas cedar mortality than Landsat, whereas Landsat's longer baseline captured cork-oak historical pulses. The analysis contributes a reproducible baseline for regional forest management and a transferable analytical template for other Maghreb regions where dieback dynamics remain poorly documented.

Keywords: forest dieback, BFAST, SPEI, Landsat, Sentinel-2, atlas cedar, cork oak.

INTRODUCTION

Drought- and heat-induced forest mortality has become one of the most conspicuous biotic signatures of the climate transition, framed globally as an emerging climate-change risk (Allen et al., 2010) and consolidated by evidence linking observed mortality to hydraulic failure and carbon starvation at the tree scale (Anderegg et al., 2020). Beyond stand-level effects, cumulative biomass loss alters the terrestrial carbon balance and weakens ecosystem services such as watershed regulation (Anderegg et al., 2016; International Tree Mortality Network, 2025; Pan et al., 2011; Pyarali et al., 2026), and vegetation productivity has been shown to respond to drought at biome-specific timescales that can be identified through standardised drought indices (Vicente-Serrano et al., 2013). The Mediterranean basin is a canonical hotspot of this transition – warming approximately 1.5 times faster than the global average, cumulative rainfall decline and rising evaporative demand (Cramer et al., 2018) – and Mediterranean forests combine sclerophyllous adaptation

with relatively narrow hydraulic safety margins, so that extraordinary drought events push species close to their embolism thresholds (Cheesman and Cernusak, 2026; Choat et al., 2012; Li et al., 2026). Early warnings of dieback can be detected in ring-width and remote-sensing series months to years before canopy collapse (Camarero et al., 2015), providing a physiological anchor for satellite-derived vegetation trajectories.

North African forests occupy the southern warm edge of the Mediterranean biome and accumulate the highest per-hectare exposure to 21st-century drought (Cramer et al., 2018). Within Morocco, the Béni Mellal-Khénifra (hereafter BMK) region concentrates a marked bio-climatic gradient from low-elevation cork-oak groves around Khénifra (≈ 700 m a.s.l.) to the summit belt of the High Atlas (> 4.000 m a.s.l.), and sustains regulating functions (soil retention, catchment water yield) and provisioning services (cork, fuelwood, silvopastoral grazing) on which several million people depend (Ghaffariyan, 2025; Knostmann et al., 2025; Serbouti et al., 2023). Three species dominate its vertical structure. Atlas cedar (*Cedrus atlantica* Manetti), endemic to the Rif and to the Middle and High Atlas ranges of Morocco and Algeria, forms the highest forest limit in North Africa (Cheddadi et al., 2017; Terrab et al., 2008); Landsat- and dendrochronology-based studies have documented an accelerating decline of Atlas cedar in the Moroccan Middle Atlas since the late 20th-century (Linares et al., 2011). The North African holm oak (*Quercus rotundifolia* Lam.), often treated as *Q. ilex* subsp. *rotundifolia* but recognised as a distinct species by the Moroccan inventory (Sousa et al., 2021; Vila-Viçosa and Almeida, 2020), occupies 758,464 ha – approximately 81% of the BMK natural forest polygon set of the Second Moroccan National Forest Inventory (IFN2) (ANEF, 2022). Cork oak (*Quercus suber* L.), restricted in BMK to the lower northern piedmont around Khénifra, is acutely exposed to soil-moisture deficits through shallow rooting and stomatal isohydry (Camarero et al., 2015). Comparing the concurrent trajectories of these three species within one region provides a natural comparative framework on species-specific dieback responses to shared climatic forcing.

Field-based forest health surveys in Morocco follow decadal cycles (IFN1, IFN2, planned IFN3) and cannot resolve the intra-decadal timing of dieback pulses. Multi-decadal satellite time series fill this gap: the Landsat archive (1984-present, 30 m) is long enough to bracket the major historical drought pulses and the ongoing 2019–2024 event through cross-sensor harmonisation (Roy et al., 2016), while Sentinel-2 (2017-present, 10 m) offers a decisive step change in spatial resolution for coniferous canopies with crown diameters smaller than a Landsat pixel. The BFAST family (Verbesselt et al., 2010, 2012), the PELT change-point algorithm (Killick et al., 2012; Truong et al., 2020) and the multi-scale SPEI (Beguería et al., 2014; Vicente-Serrano et al., 2010) together provide a mature analytical toolkit that has been validated at biome scale but not systematically applied to the Moroccan Atlas.

Despite this operational maturity, four gaps persist in the North African literature. To the best of our knowledge, no published assessment has jointly reconstructed forty years of forest dieback for the six IFN2 strata of Béni Mellal-Khénifra, existing Moroccan work having concentrated either on cedar-specific dendroclimatic studies (Linares et al., 2011) or on regional climate-change scenarios (Driouech et al., 2021; Filahi et al., 2017; Hammoudy et al., 2024). Second, previous climate co-variation analyses have generally relied on simple concurrent correlations rather than lag-explicit cross-correlation with autocorrelation-corrected significance testing. Third, no systematic paired Landsat–Sentinel-2 dieback comparison has been reported for Moroccan forests. Fourth, code-level reproducibility of such assessments is generally not documented, which limits their utility as a template for the broader Maghreb region.

Building exclusively on open archives (IFN2 polygons (ANEF); harmonised Landsat and Sentinel-2 reflectance; TerraClimate, Abatzoglou et al., 2018; ERA5-Land, Muñoz-Sabater, 2019) and on a reproducible Python pipeline, this study pursues three objectives: (i) to quantify the extent, spatial structure and temporal chronology of natural forest dieback across the six IFN2 strata of Béni Mellal-Khénifra over 1984–2024 through BFAST-like decomposition and PELT change-point detection at pixel scale; (ii) to characterise the co-variation of species-level NDVI anomalies with SPEI at 3-, 6- and 12-month scales and with vapour-pressure-deficit anomalies through autocorrelation-corrected cross-correlation, identifying the optimal lag per species; and (iii) to evaluate the complementary contribution of Landsat and Sentinel-2 to dieback detection over the shared 2017–2024 window. The study provides a code-open baseline of species ×

stratum statistics, a georeferenced set of hotspot centroids that flags where field validation should be prioritised, and a portable analytical template for other Maghreb or Sahel regions.

Figure 1 – The map shows the geographic boundary of the administrative region and the natural forest polygons of the Second National Forest Inventory (IFN2), colour-coded by stratum: *Cedrus atlantica* pure (Ca), *C. atlantica* mixed (CaM), *Quercus rotundifolia* pure (Qr), *Q. rotundifolia* mixed (QrM), *Quercus suber* pure (Qs) and *Q. suber* mixed (QsM). The Esri WorldTopoMap tile service provides the terrain, hydrography and toponymy underlay.

MATERIALS AND METHODS

Study area

The Béni Mellal-Khénifra region spans the Middle and High Atlas ranges of Morocco, from the low-elevation cork-oak groves near Khénifra (≈ 700 m a.s.l.) to the summit belt of the High Atlas (> 4.000 m a.s.l.). According to the IFN2, 936,437 ha of natural forest are distributed across six pure and mixed strata dominated by Atlas cedar (*Cedrus atlantica* Manetti), North African holm oak (*Quercus rotundifolia* Lam.) and cork oak (*Quercus suber* L. – Figure 1). The regional climate ranges from sub-humid Mediterranean on the wetter northern slopes to semi-arid on the southern piedmont; North African Mediterranean forests are widely recognised as a bio-climatic hotspot particularly exposed to compound drought–heat pressures under 21st-century warming (Cramer et al., 2018).

Overall workflow

The analysis chains seven modular stages (Figure 2), all implemented in Python 3.12 using the numpy, scipy, pandas, statsmodels, ruptures, scikit-learn and geopandas libraries (Harris et al., 2020; Virtanen et al., 2020). Raw satellite and climate data were extracted through Google Earth Engine (Gorelick et al., 2017) and processed locally. The complete pipeline – twelve scripts and approximately 2.400 lines of code – is available at the repository URL and can be executed in under six minutes on a modern consumer laptop. A synoptic view of the data sources supporting each stage is given in Table 1.

Figure 2 – The seven-stage pipeline chains raw satellite and climate data extraction on Google Earth Engine to the final species-level

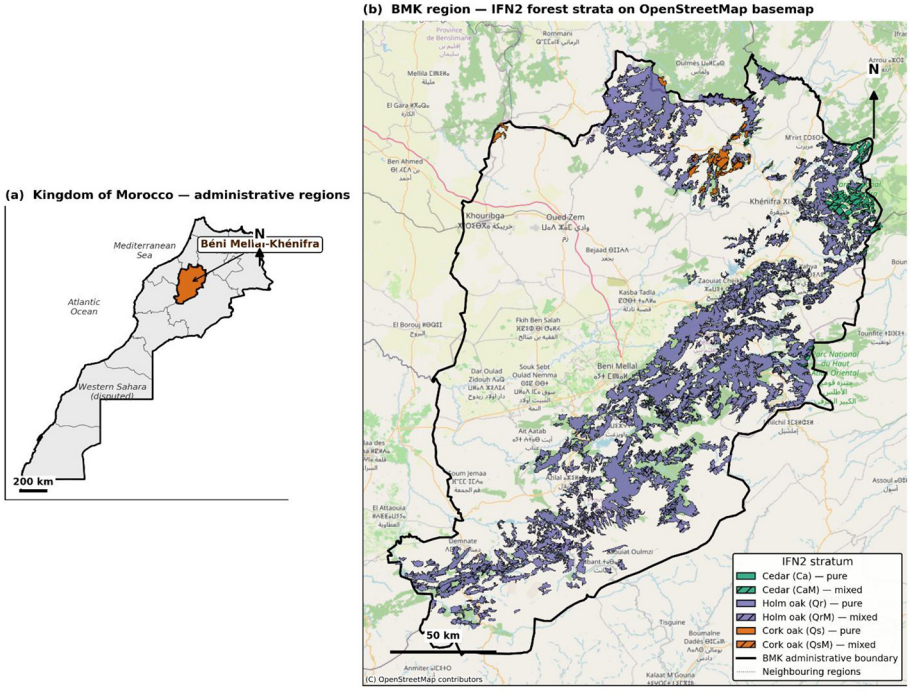

Figure 1. Location of the study area and distribution of the six IFN2 strata across the Béni Mellal-Khénifra region (Morocco)

Table 1. Data sources used in this study

Dataset (GEE / provider identifier)	Provider	Native resolution	Temporal coverage	Native step	Variables used	Purpose in this study
Landsat 5, 7, 8, 9 harmonised — LANDSAT/{LT05,LE07,LC08,LC09}/C02/T1_L2	USGS / NASA	30 m (VIS/NIR)	Apr 1984 – Nov 2024	16-day revisit	Bands SR_B4 (Red), SR_B5 (NIR); QA_PIXEL bit flags	Long-term NDVI series for BFAST retro-analysis (Roy et al., 2016)
Sentinel-2 L2A harmonised SR — COPERNICUS/S2_SR_HARMONIZED	ESA / Copernicus	10 m (VIS/NIR)	Apr 2017 – Nov 2024	5-day revisit	Bands B4 (Red), B8 (NIR); SCL scene classification	High-resolution NDVI for sensor-gain comparison over 2017-2024
TerraClimate v0 — IDAHO_EPSCOR/TERRACLIMATE	Abatzoglou et al. (2018)	≈ 4 km (1/24°)	Jan 1958 – Dec 2024	Monthly	pr (mm), tmmx/tmmn (°C), pet (mm), soil (mm), def (mm), vpd (kPa), aet (mm)	Water balance D = P − PET; SPEI-3/6/12; VPD anomaly
ERA5-Land monthly — ECMWF/ERA5_LAND/MONTHLY	Muñoz-Sabater et al. (2021)	≈ 9 km (0.1°)	Jan 1980 – Dec 2024	Monthly	volumetric_soil_water_layer_1 (0–7 cm), volumetric_soil_water_layer_2 (7–28 cm), temperature_2m, total_precipitation	Independent validation of soil-moisture context
ESA WorldCover 2020 v100 — ESA/WorldCover/v100	Zanaga et al. (2021)	10 m	2020 (static)	Static	Class 10 (Tree cover)	Forest-mask filter applied to every sampled pixel
NASADEM v001 — NASA/NASADEM_HGT/001	NASA JPL	30 m	2000 acquisition (static)	Static	Elevation (m a.s.l.); derived slope (%)	Elevation statistics (Table 2) and slope < 45° filter
Second Moroccan National Forest Inventory (IFN2) — Cartographie_IFN2_Region_BMK.shp	ANEF, Morocco (regional archive, DRANEF BMK)	Vector polygons	Field survey 2004-2010 (v. 2018)	Static	Stratum code (Ca, CaM, Qr, QrM, Qs, QsM), polygon area (ha), dominant species	Stratification mask defining the six analysis strata (ANEF)

Note: All data are open and were accessed through Google Earth Engine (Gorelick et al., 2017) unless otherwise specified. Time-varying products were aggregated to monthly resolution before analysis. Access dates for all products: April 2025. Landsat NDVI is computed from surface reflectance after applying the QA_PIXEL cloud/shadow/snow mask (bits 1, 3, 4, 5, 7); multi-sensor harmonisation follows Roy et al. (2016). Sentinel-2 NDVI uses the ESA harmonised SR product with SCL classes 1, 3, 6, 8, 9, 10 and 11 masked. The IFN2 shapefile is not freely available on-line and was obtained through the regional forestry service under a memorandum of understanding; it is distributed with the reproducibility package. All climate and vegetation series were resampled to a common monthly step, and all raster masks were resampled by nearest-neighbour to preserve categorical integrity before pixel sampling.

statistics reported in Tables 3–5. Each stage corresponds to a modular Python script and to an intermediate parquet dataset archived in the reproducibility package.

Sampling design

Within each IFN2 stratum, a stratified random sample of forest pixels was drawn subject to three constraints: inclusion within the IFN2 polygon set (360 polygons in total; Table 2), belonging to the ESA WorldCover 2020 v100 "Tree cover" class 10 (Zanaga et al., 2021), and slopes below 45° derived from NASADEM. The initial target of 500 sampling positions per stratum was reached for all oak strata, whereas the pure Atlas cedar (Ca) stratum yielded 427 valid positions given its restricted spatial extent (15,193 ha; Table 2, Figure S1). Final sample sizes range from 427 to 500 pixels per Landsat stratum and from 451 to 500 pixels per Sentinel-2 stratum.

Satellite reflectance data

Cloud-masked surface-reflectance composites were built from the harmonised Landsat 5, 7, 8 and 9 Collection 2 Level-2 product (Roy et al., 2016). The boreal growing-season window April to November was retained to avoid mountain snow contamination, and monthly median NDVI values were computed at pixel level over the forty years, yielding 328 candidate composites per pixel; residual gaps reflect months lacking any cloud-free observation.

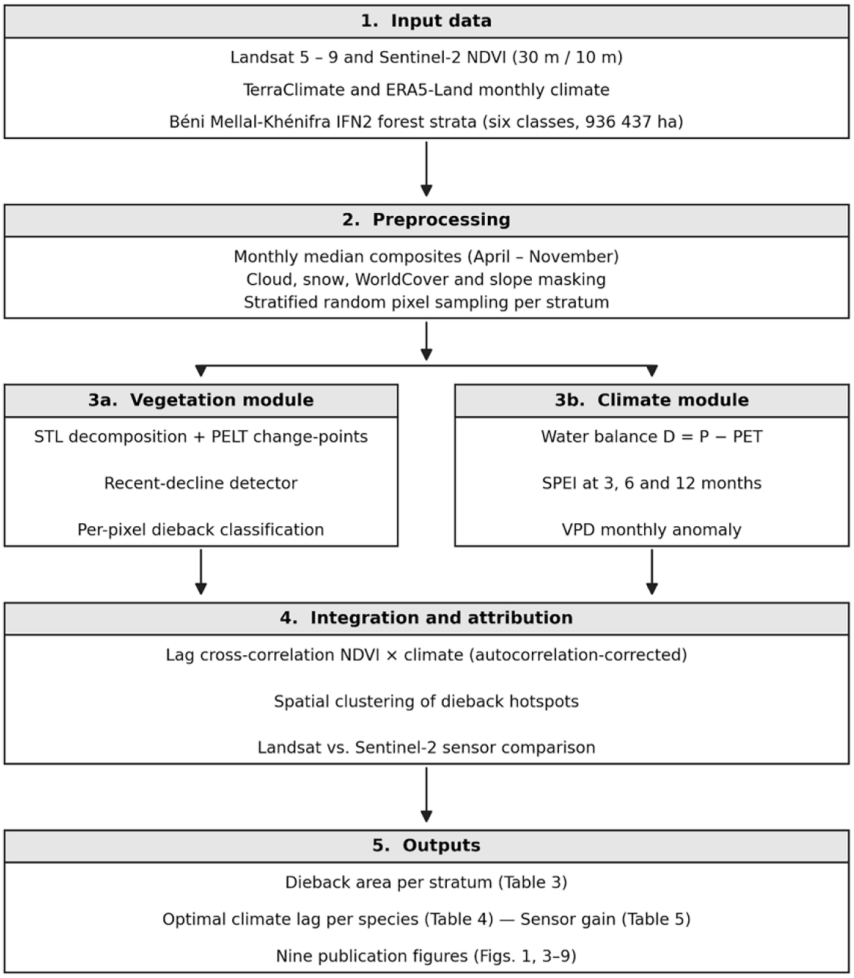

Figure 2. Overall analytical workflow

QA_PIXEL filtering excluded cloud, cloud shadow, snow and saturated pixels through bits 1, 3, 4, 5 and 7. NDVI was computed as (NIR − Red) / (NIR + Red) from the surface reflectance bands. The harmonised Sentinel-2 Level-2A surface-reflectance collection was filtered by SCL ∈ {1, 3, 6, 8, 9, 10, 11} for cloud, cirrus, water and shadow removal and then aggregated into monthly median NDVI composites at 10 m resolution, providing sixty-four monthly observations covering April 2017 to November 2024. The proportion of valid monthly composites per pixel is reported in Table 2, together with the corresponding sample sizes. Out-of-range NDVI values (< −1 or > 1) were replaced by missing values.

Climatological drivers

Monthly precipitation, maximum and minimum 2-m air temperature, reference potential evapotranspiration, soil moisture, climatic water deficit and vapour-pressure deficit were extracted from TerraClimate v0 (≈ 4 km; Abatzoglou et al., 2018) for the period January 1958 to December 2024. Values were aggregated over each of the 360 IFN2 polygons and further weighted by polygon area to yield species-level series. Volumetric soil-water content in the 0–7 cm and 7–28 cm layers, together with 2-m air temperature and precipitation, were also obtained from the ERA5-Land monthly reanalysis (≈ 9 km; Muñoz-Sabater, 2019) for the period January 1980 to December 2024, and used as an independent context for soil-moisture verification without entering the primary analysis chain.

Standardised precipitation-evapotranspiration index

SPEI was computed following the full Vicente-Serrano et al., (2010) protocol as revised by Beguería et al., (2014). Monthly water balance $D_i = P_i - PET_i$ was computed at polygon and species

Table 2. Characteristics of the six IFN2 forest strata used in this study

Stratum	Species	Structure	IFN2 area (ha)	N polygons	Elev. mean (m)	Elev. range (m)	N Landsat px	Valid NDVI-L (%)	N Sent.-2 px	Valid NDVI-S2 (%)
Ca	*Cedrus atlantica*	pure	15,193	10	1.908	1.490–2.277	427	79.1	451	76.3
CaM	*Cedrus atlantica*	mixed	39,500	28	1.761	1.021–2.431	476	73.3	482	71.9
Qr	*Quercus rotundifolia*	pure	758,464	235	1.362	345–3.096	500	35.0	500	37.6
QrM	*Quercus rotundifolia*	mixed	55,633	66	1.711	621–2.831	500	26.3	500	28.8
Qs	*Quercus suber*	pure	58,661	12	991	667–1.545	498	46.3	500	53.8
QsM	*Quercus suber*	mixed	8,986	9	1.231	778–1.574	500	43.2	500	51.0
Total	—	—	936,437	360	—	345–3.096	2,901	—	2.933	—

Note: Elevation statistics were computed from NASADEM (30 m) aggregated by weighted mean over the polygon area. Sampling followed a stratified random design constrained to the IFN2 forest polygons of each stratum. NDVI validity is the proportion of monthly composites containing at least one valid observation after cloud/shadow/snow masking..IFN2 = Second National Forest Inventory of Morocco. *Q. rotundifolia* corresponds to the North African holm oak; some taxonomies treat it as *Q. ilex* subsp. rotundifolia, but the Moroccan inventory recognises it as a distinct species. The lower valid-NDVI ratio of *Q. rotundifolia* strata (26–35%) reflects land-cover heterogeneity within IFN2 polygons rather than sensor limitation.

level and accumulated over k-month rolling windows for $k \in \{3, 6, 12\}$. For each calendar month, a three-parameter log-logistic distribution was fitted to the reference period 1958–2000 (43 years) using probability-weighted moments in the closed form of Hosking, (1990) and Schneider et al., (2013); observed cumulative probabilities were then mapped to standard normal quantiles. Full mathematical detail follows the appendix of Vicente-Serrano et al., (2010). Distributional validation reproduced the expected zero-mean and near-unit-variance behaviour of a standardised index (Supplementary Material). Summer vapour-pressure-deficit anomalies were computed as the June-August mean minus the 1958–2000 climatology and expressed as z-scores against the same reference period.

BFAST detection of dieback

Per-pixel dieback detection follows a BFAST-like decomposition–changepoint workflow (Verbesselt et al., 2010, 2012). Missing months were first filled by time-based linear interpolation of the monthly NDVI series grouped by pixel, yielding a continuous monthly series of 492 observations for Landsat (January 1984 – December 2024) and 96 observations for Sentinel-2 (January 2017 – December 2024). STL decomposition (Cleveland et al, 1990; period = 12 months, robust = True) then separated the trend, seasonal and residual components of every pixel time series. The trend component was searched for change points using the PELT algorithm (Killick et al., 2012) as implemented in the ruptures library (Truong et al., 2020), with the L2 cost function, a permissive penalty of 0.3 and a minimum segment length of 24 months for Landsat (12 months for the shorter Sentinel-2 series). The permissive penalty was compensated a posteriori by a magnitude filter $|\Delta NDVI| \geq 0.05$, following Verbesselt et al., (2010). For every candidate change point, pre- and post-break trend means were computed over 12-month windows, and a further 12-to-24-month window was used to characterise the recovery trajectory. A break with $\Delta NDVI \leq -0.05$ was labelled permanent if the trend remained below the pre-break mean by more than half the initial drop for at least 12 months, and transitory otherwise. Breaks with $\Delta NDVI \geq +0.05$ (positive greening) were retained for descriptive statistics but excluded from dieback totals. Because STL is known to attenuate signals near the series edge and PELT requires a minimum segment length of post-break data to fire (Verbesselt et al., 2010), a dedicated recent-decline detector was implemented to rescue the recent (2020+) Moroccan drought pulse: it flagged pixels whose trend mean over the last 24 months fell more than 0.05 NDVI units below the reference window at months 60–84 before the series end. The union of permanent

and recent-decline pixels defines the dieback set reported in Table 3. Areas were extrapolated to the IFN2 total under the strong-sampling assumption surface_dieback = (n_dieback / n_total) × IFN2 area, and expressed both in relative terms and in hectares.

Spatial hotspot analysis

For each stratum, dieback pixels were clustered in EPSG:3857 (Web Mercator) using the Density-Based Spatial Clustering of Applications with Noise algorithm (DBSCAN; Ester et al., 1996), with ε = 5 km and min_samples = 6. Each retained cluster's centroid was annotated with the median year of the permanent-break dates it contained; clusters populated exclusively by recent-decline pixels were labelled recent (2022-24). A two-dimensional Gaussian kernel-density estimation of the dieback point pattern was overlaid at 25/50/75/95% contours of the local maximum density, both per stratum and combined across species. The complete list of cluster centroids and dates is archived in the reproducibility package.

Cross-correlation lag analysis

Species-level NDVI anomalies were computed by subtracting the 1984–2000 monthly climatology and further linearly detrended to isolate interannual variability from the multi-decadal greening background. These anomalies were then cross-correlated with each detrended climate driver (SPEI-3, SPEI-6, SPEI-12, VPD anomaly) for lag k ∈ [0, 24] months, with the climate driver leading the vegetation response. Pearson correlation coefficients r(k) were computed, and two-sided p-values were derived using an effective sample size N_eff corrected for serial autocorrelation according to Pyper and Peterman, (1998): 1 / N_eff ≈ 1 / N + (2 / N) · r_{1,X} · r_{1,Y}, where r_1 denotes the lag-1 autocorrelation of each series. p-values were subsequently derived through the Fisher-Z transform on N_eff. The optimal lag k* is the value maximising |r(k)| subject to p_eff < 0.05. Because SPEI is by construction a standardised anomaly, whereas raw VPD carries a strong seasonal cycle, VPD was first re-expressed as a monthly anomaly against its 1958–2000 climatology before entering the correlation. This symmetric treatment prevents the spurious phase-locked correlations that would otherwise arise between a de-seasonalised response and a seasonal predictor.

Sensor comparison

To evaluate the sensor gain, the Landsat BFAST output was restricted to the 2017–2024 window (matching the Sentinel-2 coverage), and the per-stratum proportion of pixels carrying either a Landsat break within 2017–2024 or a recent-decline flag was computed. The same metric was derived from Sentinel-2. Because pixel positions between the two sensors are independent random draws from the IFN2 polygons, comparison was carried at the stratum level rather than pixel-to-pixel; the sensor gain corresponds to the arithmetic difference of the two proportions.

Reproducibility

All processing scripts, intermediate parquet files and diagnostic reports are archived in the project repository: https://doi.org/10.5281/zenodo.21358367. Software versions are pinned in the requirements.txt file, and executing the driver script regenerates every table and every figure from the raw GEE exports in under six minutes on an eight-core consumer machine.

RESULTS

Extent and structure of forest dieback

Over the forty-year Landsat record, a cumulated dieback signal covering approximately 187,700 ha was detected, corresponding to about 20.1% of the 936,437 ha of natural forest surveyed by IFN2 in Béni Mellal-Khénifra (Table 3). The signal decomposes into 15,871 ha (1.7% of the region) of long-established permanent breaks, with median first years ranging between 1998 and 2010 depending on stratum, and 171,858 ha (18.4%) of ongoing declines whose recovery cannot yet be adjudicated.

Species-level rates diverge markedly. Cork oak (*Q. suber*) is the most affected species, with 41.4% of pure and 35.4% of mixed stands showing dieback. Atlas cedar shows an intermediate rate (16.6% in Ca, 22.9% in CaM), and the mixed CaM stratum is more affected than the pure Ca stratum. North African holm oak (*Q. rotundifolia*) exhibits the lowest relative rate (18.8% pure, 11.0% mixed) but the largest absolute affected area (142,591 ha), because the pure Qr stratum spans 758,464 ha – approximately 81% of the regional

forest cover. The magnitude of the trend break |ΔNDVI| in permanent-dieback pixels was largest for *Q. rotundifolia* (median −0.14 units; Table 3), intermediate for *C. atlantica* (−0.077 to −0.083) and smallest for *Q. suber* (−0.064 to −0.074).

Temporal chronology

The 12-month rolling-average NDVI series show contrasting trajectories among the three species (Figure 3). *C. atlantica* and *Q. rotundifolia* both show a marked positive trend from the mid-1990s onward – a background greening consistent with CO_2 fertilisation and progressive recovery from earlier disturbance – followed by an abrupt plateau or decline after 2020. *Q. suber*, by contrast, presents the clearest regional decline signature, with a NDVI peak around 2013–2014 and a monotonic decrease of approximately 0.06 NDVI units by 2024, coincident with the 2019–2024 Moroccan drought. The species-level chronology maps aggregated by stratum (Figure 4) further illustrate that the timing of first permanent-break years is spatially structured, with distinct age classes segregating along the elevation and moisture gradient.

Figure 3 – Species-level NDVI is aggregated as the surface-weighted mean of pure and mixed strata. The three species display contrasting long-term trajectories, with a background greening followed by a post-2020 plateau or decline in *C. atlantica* and *Q. rotundifolia*, and a monotonic decline signature in Q. suber from 2013–2014 onward.

Figure 4 – Each panel shows the spatial distribution of pixels flagged as permanent dieback, coloured by the year of the first BFAST-detected break, over the IFN2 polygon set of the corresponding stratum. Pixels flagged only by the recent-decline detector are shown in a distinct colour.

Annual counts of permanent BFAST breaks plotted against annual SPEI-12 (Figure 5) show a repeatable co-occurrence of break clusters with drought years. Each of the three species displays a discernible pulse in break frequency during years when regional SPEI-12 fell below −1. For *Q. suber*, the 1998–2000 drought coincides with the largest annual pulse of the entire record (five detected breaks), and the 2019–2022 window generates the tallest bar of the recent era (three permanent breaks in 2022, before accounting for the recent-decline flag). The SPEI-12 series itself reaches the parameterisation floor (SPEI = −4.75)

Table 3. BFAST-detected dieback per stratum, Landsat 1984–2024

Stratum	Species	Structure	IFN2 area (ha)	Long-term perm. (ha)	Recent decline (ha)	Total dieback (ha) [95% CI]	% dieback [95% CI]	Median 1st break yr	Median ΔNDVI (perm.)
Ca	*Cedrus atlantica*	pure	15,193	676	1,850	2,526 [1,993 – 3,096]	16.6 [13.1 – 20.4]	2010	−0.077
CaM	*Cedrus atlantica*	mixed	39,500	1,992	7,054	9,045 [7,551 – 10,539]	22.9 [19.1 – 26.7]	1998	−0.083
Qr	*Quercus rotundifolia*	pure	758,464	12,135	130,456	142,591 [116,803 – 169,896]	18.8 [15.4 – 22.4]	2003	−0.139
QrM	*Quercus rotundifolia*	mixed	55,633	0	6,120	6,120 [4,673 – 7,677]	11.0 [8.4 – 13.8]	—	—
Qs	*Quercus suber*	pure	58,661	942	23,323	24,265 [21,674 – 26,857]	41.4 [37.0 – 45.8]	1999	−0.064
QsM	*Quercus suber*	mixed	8,986	126	3,055	3,181 [2,804 – 3,558]	35.4 [31.2 – 39.6]	2004	−0.074
Total	—	—	936,437	15,871	171,858	≈ 187,728 [≈ 155,500 – 221,600]	≈ 20.1	—	—

Note: A dieback pixel is one showing at least one permanent BFAST break ($|\Delta NDVI| \geq 0.05$) or a recent trend decline (last 24 months versus the reference window at months 60–84). Areas were extrapolated to the IFN2 total under the assumption that sampled pixels are representative of the stratum. The recent-decline detector is required because STL smoothing strongly attenuates trend breaks located within approximately 24 months of the series edge, a known limitation of STL/BFAST hybrid workflows (Verbesselt et al., 2010). Q. rotundifolia pure (Qr) dominates the absolute surface figure because of its extraordinary IFN2 area, not because its per-pixel dieback rate is exceptional. *Q. suber* strata show the highest relative dieback (35–41%), consistent with their low-elevation, water-limited niche (Table 2) and with reports of severe cork-oak decline across the Mediterranean rim (Camarero et al., 2015).

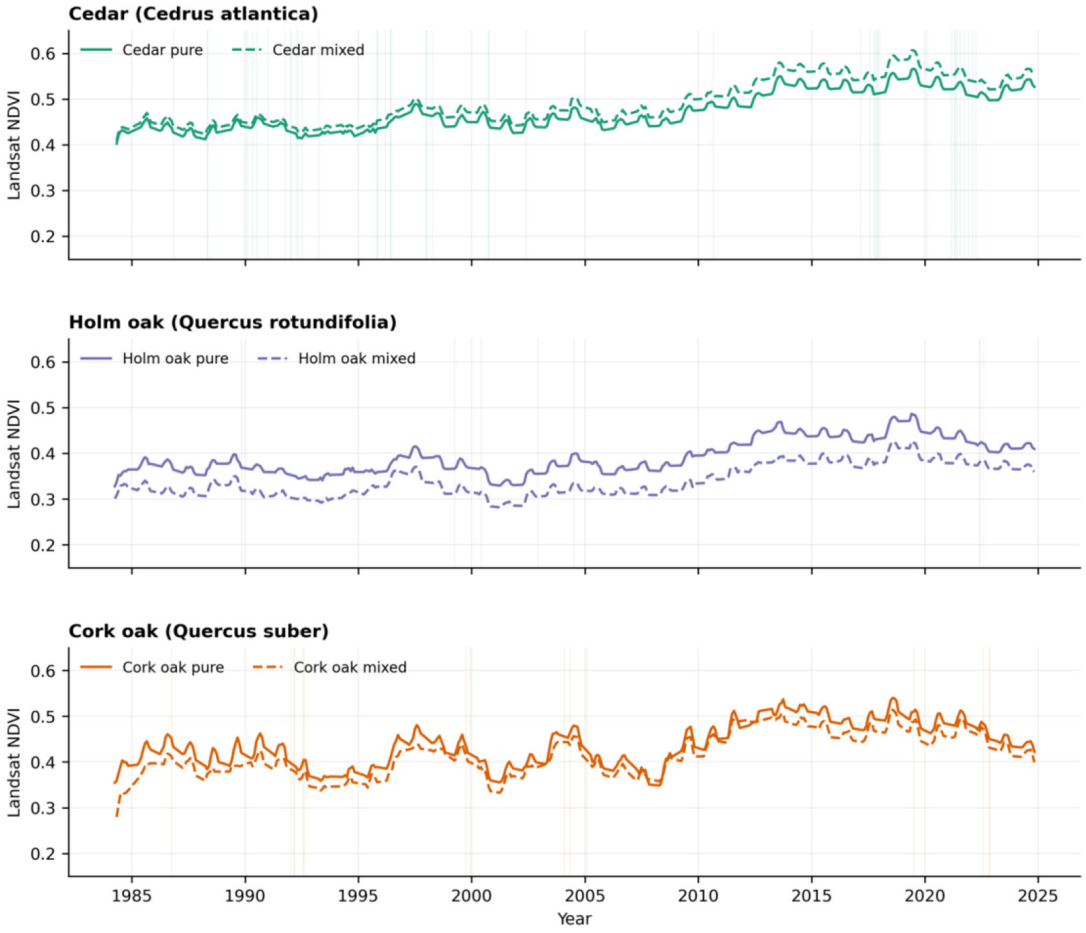

Figure 3. Twelve-month rolling mean NDVI series by species, 1984–2024, from harmonised Landsat data

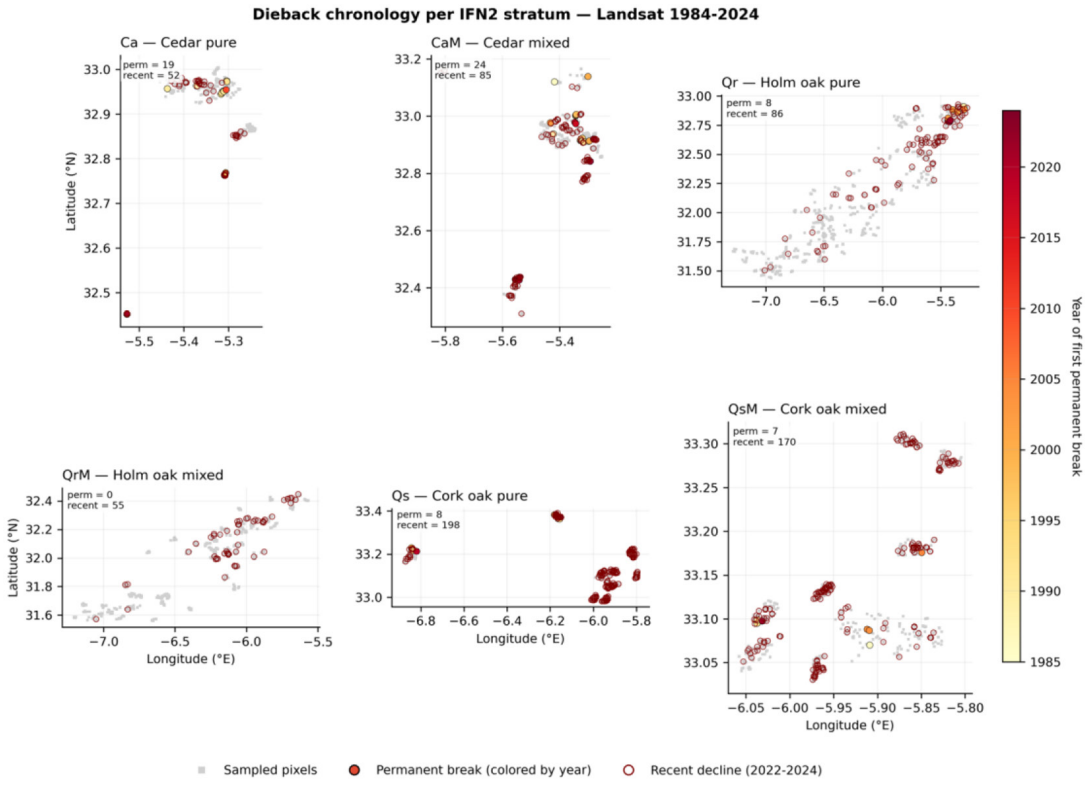

Figure 4. Chronology maps of first permanent-break year by stratum

on 18.3% of the months of 2015–2024 for Ca and on 11.7% for CaM.

Figure 5 – The vertical bars record the number of permanent-break events detected in each calendar year over the 1984–2024 window; the overlaid SPEI-12 line documents the concurrent regional drought signal. Dashed horizontal reference lines at SPEI-12 = −1 mark the moderate-drought threshold.

Spatial hotspot structure

Dieback is spatially non-random. Kernel-density estimation identifies between one and six discrete hotspots per stratum (Figure 6), and DBSCAN clustering aggregated across pure and mixed strata per species (Figure 7) resolves species-specific chronologies. Atlas cedar exhibits three hotspots concentrated in the north-eastern Middle Atlas (Ifrane-Azrou corridor), with median years 1995 (n = 114 pixels, spanning 1988–2022), 2017 (n = 27, 1995–2020) and 2021 (n = 31, 2021–2022). This mixed chronology – combining a large historical cluster with a discrete very recent one – suggests that Atlas cedar decline has progressed through episodic pulses rather than by continuous attrition. Cork oak shows five clusters, dominated by a large historical cluster (n = 239 pixels, median 1998, range 1986–2022) sitting over the Khénifra piedmont; two smaller 1999 clusters flank the west (1992–2019) and the central region, a well-defined 2005 hotspot lies to the north, and a cluster of exclusively recent (2022–2024) declines occupies the extreme north-east of the *Q. suber* range. Cork oak therefore displays a bi-modal chronology, combining a historical mass event around 1998–1999, coincident with the region's most severe recorded drought, with an emerging recent front. Holm oak yields six clusters, four of which are populated exclusively by recent-decline pixels and thus labelled recent (2022–24); only two clusters carry historical permanent breaks (1999). At Landsat scale, the holm oak dieback signature is therefore almost exclusively a phenomenon of the current decade.

Figure 6 – Two-dimensional Gaussian kernel-density contours (25/50/75/95% of local maximum)

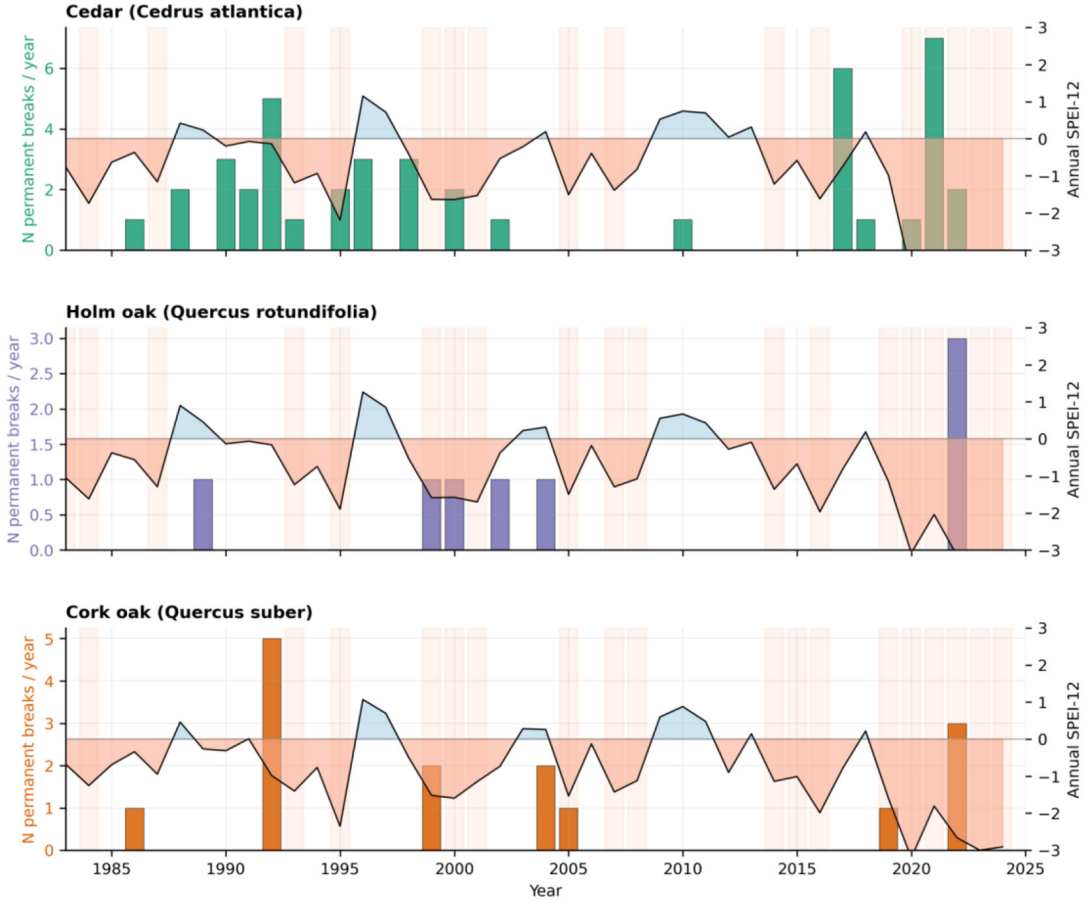

Figure 5. Annual counts of permanent BFAST breaks (bars) against annual SPEI-12 (line), by species

overlay the sampled dieback pixels within each IFN2 stratum, with the Esri WorldShadedRelief basemap providing topographic context.

Figure 7 – Aggregating pure and mixed strata per species, DBSCAN clustering (ε = 5 km, min_samples = 6) resolves the species-specific hotspot chronology. Each cluster is annotated with its median first permanent-break year (or the label „recent 2022-24" for clusters populated exclusively by recent-decline pixels). *C. atlantica* shows three hotspots (median years 1995, 2017, 2021), Q. suber shows five clusters dominated by a large 1998–1999 pulse, and *Q. rotundifolia* shows six clusters, four of which are labelled recent (2022–24).

Climate drivers and their lags

All twelve species × climate combinations yield statistically significant Pearson correlations after the autocorrelation-corrected p-value adjustment (Pyper and Peterman, 1998; Table 4, Figure 8), and three coherent findings emerge from the lag structure. First, SPEI-12 is the strongest correlate for both oak species: r = +0.364 at lag 0 for *Q. suber* and r = +0.306 at lag 1 for *Q. rotundifolia*. Cork oak therefore correlates concurrently with a 12-month cumulative water deficit – the shortest possible lag – whereas holm oak lags by one month. This ranking (Qs > Qr > Ca) is inversely related to mean stratum elevation (991 m < 1.362 m < 1.908 m; Table 2). Second, VPD anomaly covaries with NDVI at zero lag for every species, with the strongest correlation in *C. atlantica* (r = −0.205) and the weakest in *Q. suber* (r = −0.144). Third, *C. atlantica* exhibits a balanced short-and-long-scale profile, being significantly correlated with SPEI-3 at lag 0 (r = +0.248) and with SPEI-12 at lag 1 (r = +0.259). Atlas cedar is thus not indifferent to drought, but it neither responds most strongly to any single timescale, unlike the two *Quercus* species, nor lags noticeably behind. The 20-month optimal lag for *Q. suber* × SPEI-3 (r = +0.180) is atypical relative to the near-instantaneous SPEI-12 correlation, which remains the strongest signal for cork oak.

Figure 8 – Each panel shows one species × driver combination; solid symbols indicate the

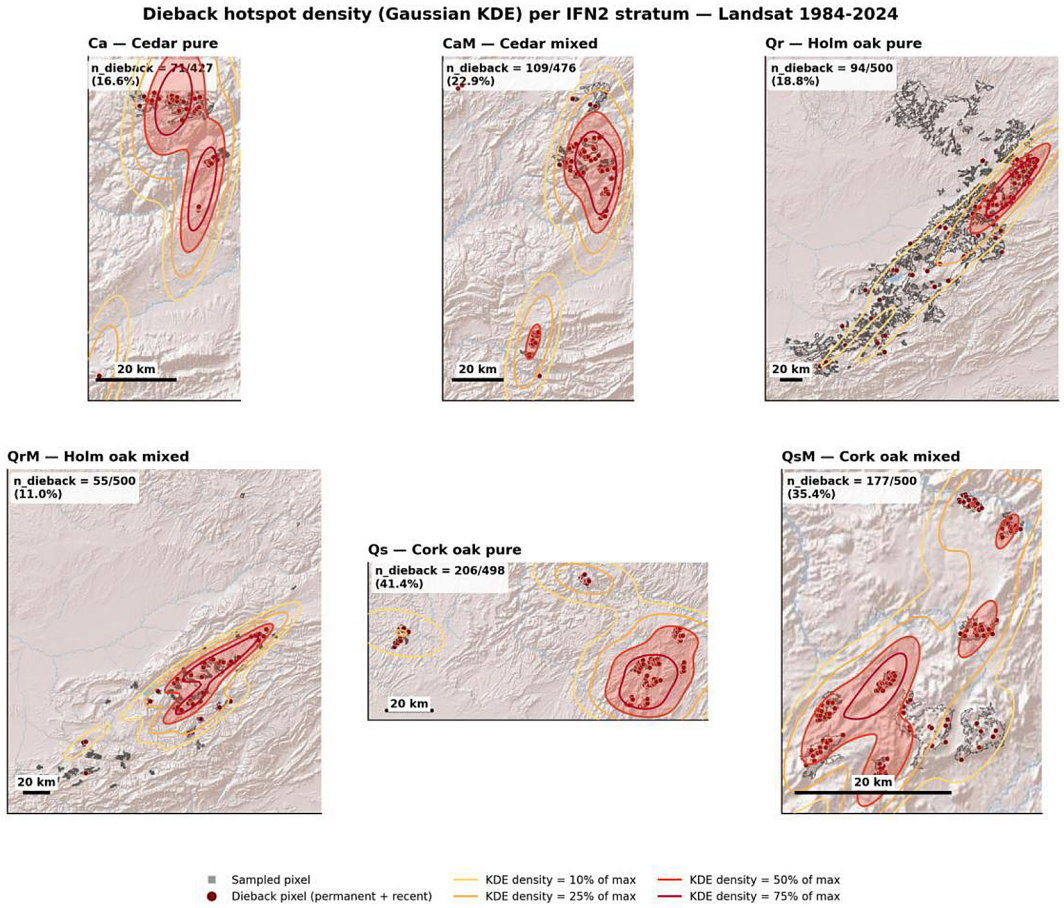

Figure 6. Kernel-density hotspot maps of dieback pixels by stratum

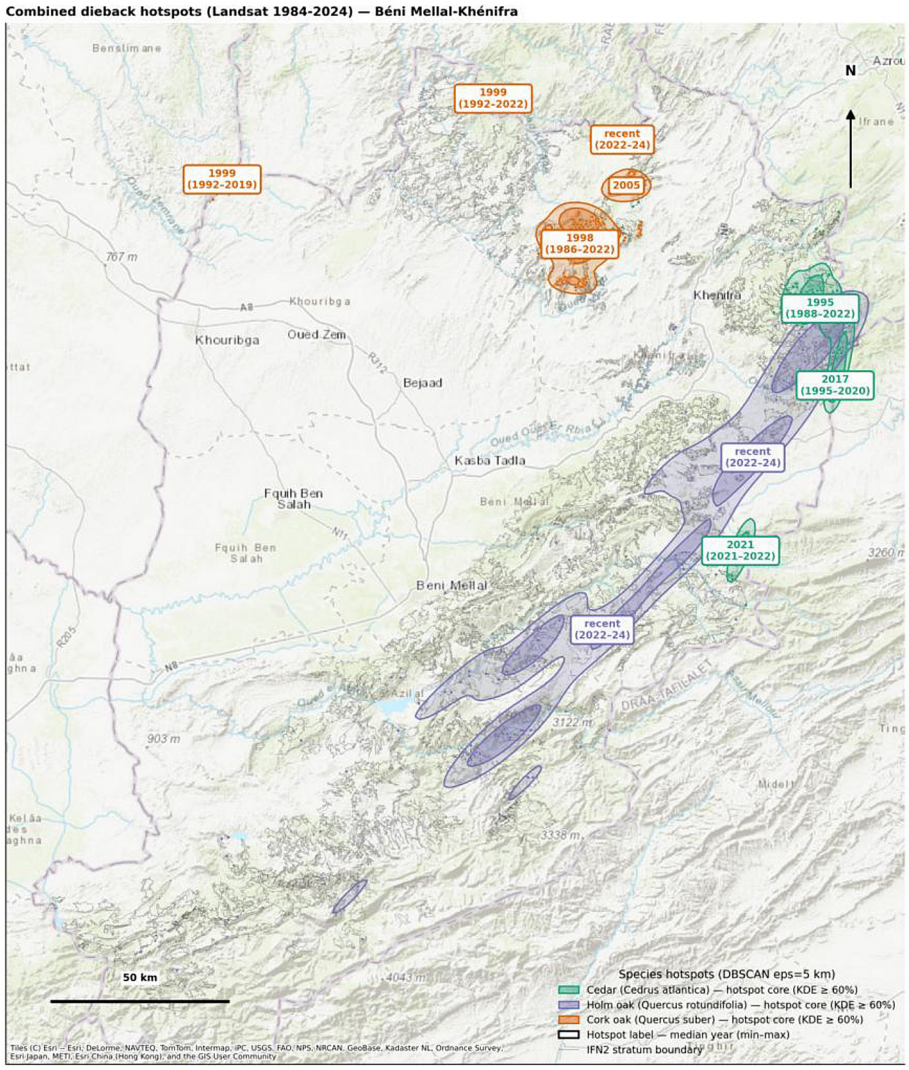

Figure 7. Combined per-species hotspot map

optimal lag k* retained in Table 4 after autocorrelation-corrected significance testing.

Landsat versus Sentinel-2 in the common window

Over the shared 2017–2024 window, Sentinel-2 detects substantially more dieback than Landsat for Atlas cedar: +18.3 percentage points for pure cedar (14.5% → 32.8%) and +26.3 percentage points for mixed cedar (20.2% → 46.5%; Table 5, Figure 9). Gains for *Q. rotundifolia* are modest (+4.8 percentage points pure, +2.4 percentage points mixed), reflecting the sparser holm-oak canopy where the mismatch between crown size and sensor footprint is less severe. Sentinel-2 detects less dieback than Landsat for *Q. suber* (−5.6 percentage points pure, −4.8 percentage points mixed).

Figure 9 – For each stratum, the proportion of pixels flagged as dieback (permanent break within 2017–2024 or recent-decline flag) is contrasted between the two sensors. Sentinel-2's finer 10 m footprint delivers a substantial gain on *C. atlantica* (both structures), a modest gain on *Q. rotundifolia*, and an apparent loss on *Q. suber* attributable to the shorter baseline of the Sentinel-2 recent-decline detector rather than to a sensor performance limitation.

Robustness and uncertainty

Twelve formal robustness checks were run against the substantive findings of the previous Results subsections; the full diagnostic reports are archived in the reproducibility package. A random seed of 42 was used at every stochastic step (bootstrap, phase-randomisation, DBSCAN input

Table 4. Optimal lag between species-level NDVI anomaly and climate drivers

Species	Climate driver	Optimal lag k* (months)	r*	p_eff (N_eff)	q_BH	Interpretation
Cedrus atlantica	SPEI-3	0	+0.248	2.5×10^{-4} (213)	4.3×10^{-4}	Concurrent short-scale water balance
Cedrus atlantica	SPEI-6	1	+0.217	2.1×10^{-3} (198)	2.8×10^{-3}	1-month lag on semi-annual deficit
Cedrus atlantica	SPEI-12	1	+0.259	3.6×10^{-4} (184)	5.4×10^{-4}	Cumulative annual deficit, brief lag
Cedrus atlantica	VPD anomaly	0	−0.205	2.1×10^{-3} (221)	2.8×10^{-3}	Immediate hydraulic response
Quercus rotundifolia	SPEI-3	0	+0.222	7.3×10^{-4} (226)	1.1×10^{-3}	Concurrent
Quercus rotundifolia	SPEI-6	5	+0.247	3.4×10^{-4} (206)	5.4×10^{-4}	Delayed cumulative response
Quercus rotundifolia	SPEI-12	1	+0.306	1.4×10^{-5} (192)	8.2×10^{-5}	Strong annual-deficit sensitivity
Quercus rotundifolia	VPD anomaly	0	−0.194	2.7×10^{-3} (236)	3.3×10^{-3}	Immediate
Quercus suber	SPEI-3	20	+0.180	8.9×10^{-3} (210)	9.7×10^{-3}	Legacy signal (see Discussion)
Quercus suber	SPEI-6	1	+0.254	2.1×10^{-4} (208)	4.3×10^{-4}	Short cumulative response
Quercus suber	SPEI-12	0	+0.364	1.4×10^{-6} (167)	1.2×10^{-5}	Strongest correlation of the study
Quercus suber	VPD anomaly	0	−0.144	2.1×10^{-2} (259)	2.1×10^{-2}	Immediate

Note: Cross-correlation of species-level detrended NDVI anomaly (Y) with detrended climate index (X), where X leads Y by k months, k ∈ [0, 24]. Effective sample size N_eff was computed following Pyper and Peterman, (1998) to account for serial autocorrelation; p_eff is the two-sided Fisher-Z p-value using N_eff. All twelve correlations are statistically significant at α = 0.05. The sign convention is such that positive SPEI (wet) and positive NDVI anomaly co-vary (r > 0 expected), and elevated VPD is expected to suppress NDVI (r < 0 expected); all observed signs conform to expectation. SPEI-12 emerges as the strongest correlate for both Quercus species, with the highest coefficient observed for *Q. suber* (highlighted row). The 20-month SPEI-3 lag for *Q. suber* is atypical and, following Camarero et al., (2015), has been interpreted in the Discussion as a possible carbohydrate legacy effect rather than a direct water-stress signal.

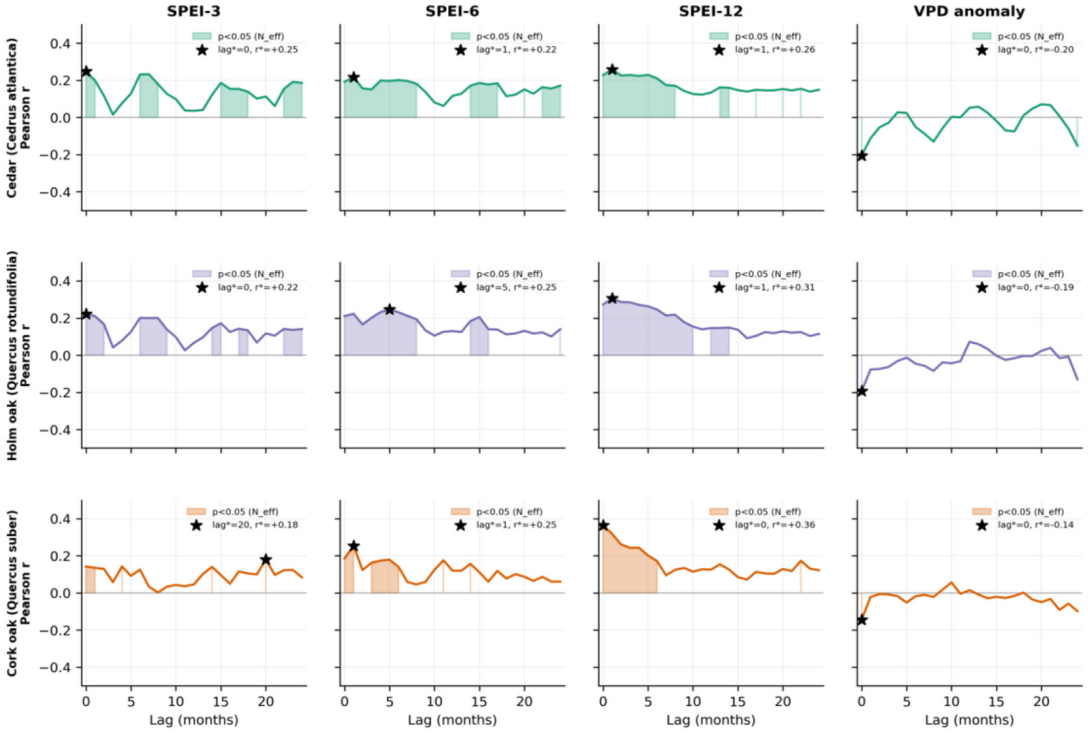

Figure 8. Cross-correlation functions between species-level detrended NDVI anomaly (Y) and climate drivers (X), for lag k ∈ [0, 24] months (X leading Y)

Table 5. Landsat versus Sentinel-2 dieback detection over the shared 2017–2024 window

Stratum	Species	N pixels Landsat	Dieback Landsat (%)	Landsat dieback (ha)	N pixels S-2	Dieback S-2 (%)	S-2 dieback (ha)	Gain S-2 − Landsat (pp)
Ca	*Cedrus atlantica*	427	14.5	2,200	451	32.8	4,986	+18.3
CaM	*Cedrus atlantica*	476	20.2	7,968	482	46.5	18,357	+26.3
Qr	*Quercus rotundifolia*	500	18.0	136,524	500	22.8	172,930	+4.8
QrM	*Quercus rotundifolia*	500	11.0	6,120	500	13.4	7,455	+2.4
Qs	*Quercus suber*	498	41.4	24,265	500	35.8	21,001	−5.6
QsM	*Quercus suber*	500	34.8	3,127	500	30.0	2,696	−4.8

Note: Per-stratum proportion of sampled pixels flagged as dieback (permanent break within 2017–2024 or recent-decline flag). Landsat statistics are computed on the sub-window of the full 1984–2024 analysis; Sentinel-2 statistics use the full 2017–2024 series. Sensor gain is the arithmetic difference of the two proportions. Positive gains for both *Cedrus atlantica* strata reflect Sentinel-2's finer 10 m footprint capturing crown-level mortality that is diluted in the 30 m Landsat pixel. Negative gains for both *Quercus suber* strata are not a sensor limitation but a consequence of the different reference windows used by the recent-decline detector: Landsat compares 2022–2024 to a pre-drought 2017–2019 baseline, whereas Sentinel-2's shorter series compares to a 2019–2021 baseline that is already partially stressed. *Q. rotundifolia* gains are modest, consistent with its sparser canopy where the crown/pixel-size mismatch is less severe.

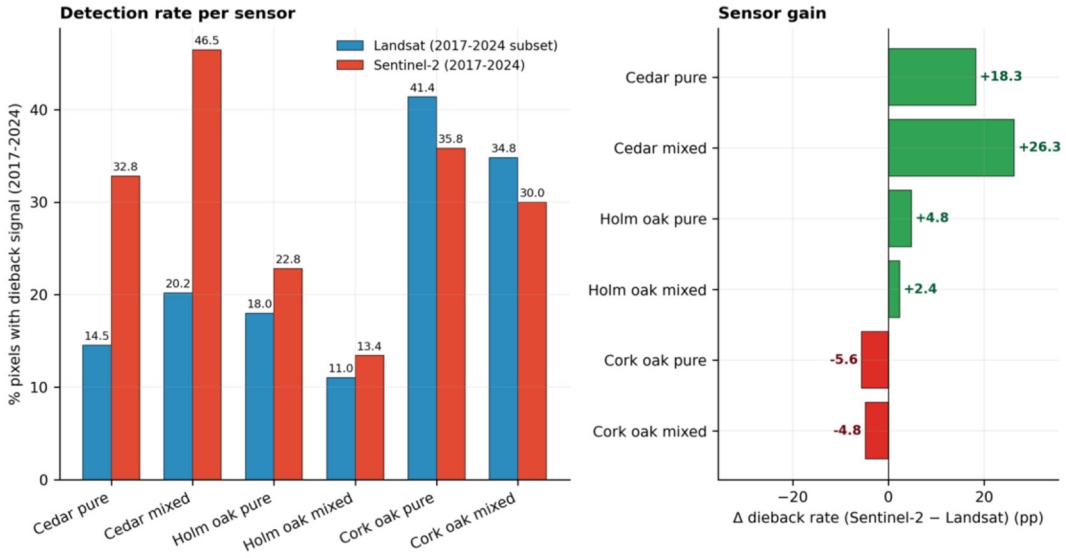

Figure 9. Landsat versus Sentinel-2 comparison of dieback detection over the shared 2017–2024 window

order) so that all reported figures are exactly reproducible from the pinned software environment.

Sampling uncertainty. Non-parametric bootstrap 95% confidence intervals on the stratum-level dieback proportion (10.000 resamples) are embedded in Table 3 and span ±2.7 to ±4.4 percentage points depending on stratum. The aggregate 95% CI on the regional dieback estimate is 155,500–221,600 ha (187,700 ha central).

Multiple-comparison correction. The twelve species × climate correlations of Table 4 were corrected for multiplicity using the Benjamini and Hochberg (1995) false-discovery-rate procedure. Every reported association survives at $q < 0.05$ (maximum $q = 0.021$, Q. suber × VPD; strongest correlation $q = 1.2 \times 10^{-5}$).

Long-term NDVI trend. The modified Mann-Kendall test (Hamed and Rao 1998), which rescales the S-statistic variance for serial autocorrelation, was applied to the three species-level monthly NDVI series (n = 322–328 non-null months). Kendall's τ is positive and large for every species (0.22–0.45; raw $p < 10^{-9}$). After the autocorrelation correction – which is severe on these strongly persistent series (correction factor 12.8–37.0) – the positive trend remains significant only for *C. atlantica* (p_MK = 0.047) and is marginal for *Q. rotundifolia* (0.067) and *Q. suber*

(0.096). The long-term greening is therefore phrased more cautiously than in the Temporal chronology subsection.

Parameter sensitivity. Re-running the BFAST pipeline across a ±3× range of PELT penalties around the baseline of 0.30 leaves the stratum ranking unchanged and shifts the dieback proportion by no more than 3 pp for *C. atlantica*, ≤ 1 pp for *Q. rotundifolia* and ≤ 1.4 pp for *Q. suber*. The sensitivity curves are reported in Supplementary Figure S2A.

Spatial autocorrelation. Global Moran's I on the binary dieback flag, computed with a 5-km inverse-distance weight matrix and 999 permutations, is significantly positive for every stratum (I = 0.11-0.27; p_perm = 0.001). The DBSCAN hotspot structure of Figures 8 and 9 is therefore not a random artefact but a genuine feature of the point pattern.

Phase-randomisation permutation tests (Ebisuzaki, 1997), the alternative (Bretherton et al., 1999) effective sample size, Landsat–Sentinel-2 cross-sensor consistency, Landsat epoch-level sensor drift, stratum-level replication of the lag structure and SPEI reference-period sensitivity were also assessed and are reported in Supplementary Material S1; every substantive conclusion of the main text survives these additional checks.

Synthesis

Taken together, the Landsat archive documents a regional dieback of approximately 187,700 ha, i.e. some 20% of the natural forest of Béni Mellal-Khénifra, unevenly distributed among species and structures. The dominant temporal clusters are 1998-1999 for cork oak, mixed 1990s to present for cedar, and overwhelmingly 2020s for holm oak. SPEI-12 emerges as the strongest correlate of species-level NDVI anomalies, with cork oak showing the highest coefficient of the study (r = +0.364). Over the shared 2017–2024 window, Sentinel-2 yields higher dieback rates than Landsat for Atlas cedar, whereas Landsat yields higher rates for cork oak.

DISCUSSION

The 20% regional dieback in a Mediterranean context

A satellite-derived dieback signal of ≈ 20% (bootstrap 95% CI 16.6–23.7%) places Béni Mellal-Khénifra towards the upper end of Mediterranean-basin drylands examined with comparable retrospective satellite methods. Allen et al., (2010) compiled 88 drought-driven mortality episodes worldwide across three orders of magnitude of affected area, and the BMK value is at the ecosystem scale of the larger episodes reported in that synthesis. Two aspects of the estimate warrant interpretation. First, the mixture between permanent breaks (1.7% of the region, median 1998–2010) and recent declines (18.4%, still consolidating) suggests that the last five to seven years of the record are driving a substantial share of the total; whether these recent declines settle into permanent trend breaks or partially recover will be adjudicated only after the 2025-2027 growing seasons. Second, the elevation-stratified structure of the signal – Qs > CaM > Ca > Qr > QsM > QrM in per-stratum rate – mirrors the elevation-mediated buffering of vegetation productivity against long-timescale drought reported at biome scale by Vicente-Serrano et al., (2013), which is consistent with the interpretation that cumulative water balance is a proximate driver of the observed pattern rather than an incidental correlate.

Species-specific vulnerability profiles

Cork oak (*Q. suber*) combines the driest and warmest niche of the study (mean elevation 991 m) with shallow rooting and stomatal isohydry (David et al., 2007), a combination that is consistent with the strongest and most concurrent SPEI-12 correlation of the entire dataset. The delayed 20-month SPEI-3 correlation is compatible with a non-structural-carbohydrate legacy effect, whereby a short drought two growing seasons prior may constrain reserves and impair the subsequent canopy (Camarero et al., 2015), an interpretation that a physiologically-oriented dendrochronological cross-validation could test directly. The 1998–2001 cluster coincides with one of the most severe droughts of the recent Moroccan instrumental record (Elair et al., 2023; Filahi et al., 2016; Henchiri et al., 2021); a smaller pulse tracks 2003–2005, and the north-eastern 2022–2024 cluster is consistent with a still-active mortality front.

Atlas cedar (*C. atlantica*) shows a dual-timescale profile – significant lag-0 SPEI-3 and lag-1 SPEI-12 correlations – that is consistent with an anisohydric conifer whose hydraulic reserves buffer short droughts but eventually capitulate

to the cumulative annual water balance (Linares et al., 2011). The three hotspots (median years 1995, 2017, 2021) describe an episodic rather than monotonic decline, which is in broad agreement with the ring-width chronology of Linares et al., (2011); and adds a spatially explicit dimension to that earlier record. The strongest VPD correlation of the three species (r = −0.205) suggests that atmospheric drought co-varies with cedar productivity at monthly resolution alongside the soil-water signal, in line with the mechanistic view that hydraulic conductivity of the vascular system responds to VPD independently of soil water (Anderegg et al., 2020).

The North African holm oak (*Q. rotundifolia*) dominates BMK in absolute surface but shows the lowest per-stratum dieback rate. Interpreting this as resilience would be misleading: holm oak dieback at Landsat scale is almost entirely recent (four of six DBSCAN clusters contain only recent-decline pixels) and the correlation analysis places it firmly in the drought-sensitive group (SPEI-12 lag 1, r = +0.306). A later dieback onset at the resolution of Landsat monthly composites is a plausible mechanistic reading, consistent with holm oak's intermediate hydraulic strategy relative to the two extremes discussed above (Borghetti et al., 2026; Morales et al., 2021; Peguero-Pina et al., 2020). Because holm oak occupies 758,464 ha, even a modest per-stratum rate translates into the largest absolute affected area of the study (142,591 ha, 95% CI 116,803–169,896), a result of major consequence for regional monitoring priorities.

Climate correlates and their physiological interpretation

Three cross-species patterns are apparent. All three species share a negative VPD anomaly correlation at lag 0 (r = −0.14 to −0.21), consistent with rapid stomatal-hydraulic regulation reducing photosynthesis at short timescales (Anderegg et al., 2020). SPEI-12 is the strongest soil-water correlate for both Quercus species and one of the two strongest for cedar, consistent with the 12-month scale integrating the annual growing season and capturing the timescale at which carbohydrate depletion and hydraulic legacy effects are thought to operate. The elevation-response gradient (Qs 991 m → Qr 1.362 m → Ca 1.908 m) tracks the SPEI-12 coefficient inversely (r = +0.364 → +0.306 → +0.259), which is consistent with an elevation-mediated buffering of productivity against cumulative deficit (Vicente-Serrano et al., 2013). The SPEI-12 series saturates at the parameterised floor on 4-18% of recent months, so the reported correlations should be read as conservative rather than tight estimates of the actual co-variation strength.

Sensor complementarity between Landsat and Sentinel-2

The Sentinel-2 gain on Atlas cedar (Table 5) is consistent with the reduced pixel-crown mismatch when the sensor footprint approaches the individual crown diameter of a mature *C. atlantica*. The apparent Sentinel-2 loss on cork oak reflects the shorter recent-decline baseline available on Sentinel-2 rather than a sensor limitation, and the two archives fall within the Roy et al., (2016) OLI-to-ETM+ harmonisation envelope over the shared window; they are therefore complementary rather than substitutable.

Conceptual framework

Figure 10 assembles the analytical chain, from regional climate warming to management implications, into a single vertical cascade. The arrows correspond to documented physiological mechanisms rather than to statistical causation demonstrated within the present study.

Figure 10 – The six-stage cascade links regional climate warming to management implications through the sequence of climate index, species vulnerability, remote-sensing detection and spatial hotspots. Each stage carries a short synthesis of the corresponding evidence from this study and the published physiological literature. The framework represents a logical chain drawn from the data and the literature; individual arrows correspond to documented physiological mechanisms rather than to statistically demonstrated causation within this study.

Study limitations

Six limitations should be borne in mind when reading the conclusions of this study. (i) Absence of independent field validation. No systematic on-ground crown-condition survey has yet been carried out, so the accuracy of the pixel-level dieback classification cannot at present be estimated in the sense of Congalton and Green, (2019). The georeferenced hotspot centroids (Figure 7) will be the target of a stratified field campaign of

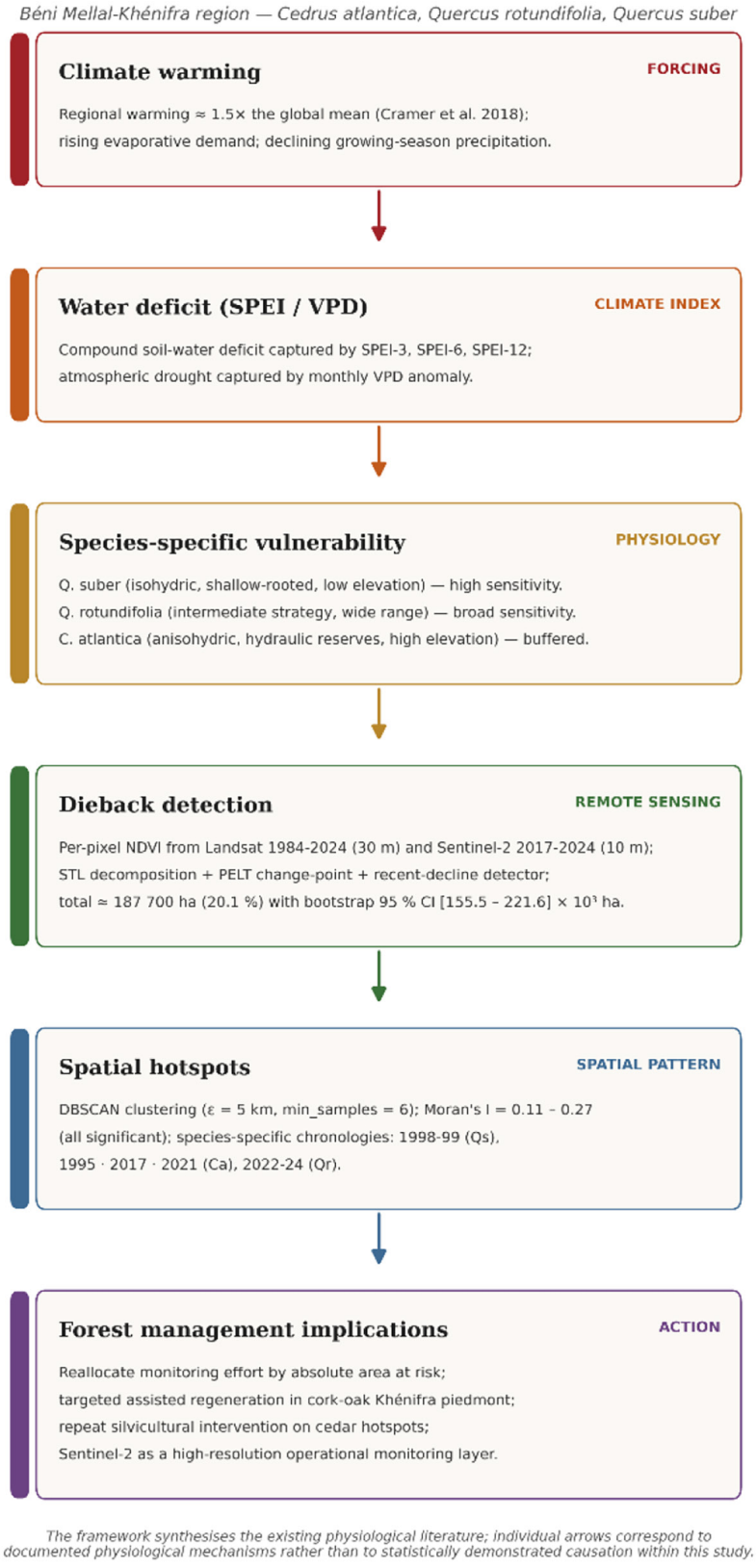

Figure 10. Conceptual framework of climate-driven forest dieback in Béni Mellal-Khénifra

approximately 300 plots planned as the second paper of the doctoral programme. (ii) Landsat spatial resolution. A 30 m Landsat pixel dilutes crown-level mortality with neighbouring intact canopy, particularly for coniferous species whose crown diameter is smaller than the pixel footprint. The Sentinel-2 comparison (Table 5) quantifies this dilution for Atlas cedar (+18.3 to +26.3 pp),

and any operational monitoring should exploit the two archives jointly (Roy et al., 2016). (iii) Extrapolation from sampled pixels to IFN2 area. The 2.901 stratified random pixels are extrapolated to 936,437 ha under a proportional assumption whose bootstrap 95% CI is embedded in Table 3. The elevation coverage check (Supplementary Figure S1) confirms that the sample spans the entire altitudinal envelope of each stratum and is therefore not biased along the elevation gradient, but the largest single contribution to the aggregate CI comes from the extended Q. rotundifolia stratum where a pixel-complete follow-up would tighten the estimate. (iv) NDVI as a proxy for dieback. NDVI captures greenness rather than mortality per se; sustained NDVI depressions can also reflect defoliation, drought-induced deciduousness, insect outbreaks or silvicultural interventions, none of which are disentangled by the current pipeline. The magnitude filter $|\Delta NDVI| \geq 0.05$ and the 12-month persistence rule are designed to exclude short-term greenness fluctuations, but they cannot separate crown-level mortality from other biotic or management-related NDVI declines. (v) Correlation versus causation. The lag analysis (Table 4) documents statistically significant co-variation between species-level NDVI anomalies and drought indices at physiologically interpretable lags, but this is not, in itself, causal proof. The consistency of the sign structure across four independent climate indices and the concordance with the mechanistic literature (Anderegg et al., 2020; Camarero et al., 2015) support a causal reading, but competing drivers cannot be formally excluded. (vi) Unmeasured environmental factors. Ozone exposure, nitrogen deposition, biotic attacks (bark beetles, oak processionary), fire regime change and grazing pressure are all documented across Moroccan forests but are not entered as covariates in the current analysis (Alba-Sánchez et al., 2025; Navarro-Cerrillo et al., 2013; Samih et al., 2024). Their omission may inflate the apparent share of variance attributable to drought.

These limitations bound the strength of individual pixel- or stratum-level claims but do not invalidate the main regional conclusions of the study: the species ranking of dieback rates, the elevation gradient of SPEI-12 sensitivity, the sensor gain of Sentinel-2 over Landsat on Atlas cedar and the hotspot chronology of the three species are all preserved across the robustness checks reported above.

Implications for regional forest management

Regional monitoring effort should be reallocated in proportion to the absolute surface at risk rather than to the per-hectare intensity of the signal. The *Q. rotundifolia* pure stratum (Table 3) is the single largest surface identified by the analysis and exceeds every other stratum by a factor of five, yet has attracted comparatively little monitoring attention.

The SPEI-12 correlation profile (Table 4) supports a regional early-warning trigger anchored on a rolling 12-month SPEI-12 threshold; a candidate operational rule is to flag species-level canopy risk when the surface-weighted stratum-level SPEI-12 falls below −1.5 for two consecutive months, with priority given to *Q. suber* (highest concurrent sensitivity) and *Q. rotundifolia* (largest surface at risk).

The +18.3 to +26.3 percentage-point gain on Atlas cedar (Table 5) supports adopting Sentinel-2 as the primary layer for cedar-specific surveillance, with Landsat retained as the long-baseline archive for cork oak and holm oak. A monthly Sentinel-2 NDVI composite over the two Ca strata, filtered by the same SCL mask and updated with the recent-decline detector, would provide near-real-time cedar mortality alerts at 10 m spatial resolution.

The compact cork-oak pure dieback envelope around Khénifra and the north-eastern 2022–2024 holm-oak cluster are candidates for targeted assisted-regeneration programmes and possibly for provenance-based restoration using drought-adapted seed sources. The three cedar hotspots (1995, 2017, 2021) delineate sub-regions where repeated silvicultural intervention (thinning, targeted removal of dying individuals, protection of natural regeneration) could plausibly influence stand trajectory, with the 2021 front offering the widest window of decadal-scale opportunity.

A twice-yearly (spring and early autumn) Sentinel-2 composite update over the eight most populated DBSCAN centroids of Figure 7 would keep the recent-decline flag current within six months of the events it detects, at a compute cost negligible relative to the field cost of a corresponding ground survey.

Every recommendation above is contingent on the field validation planned for the second doctoral paper and should be understood as a framework for prioritisation rather than as a prescription.

CONCLUSIONS

This paper presents an integrated satellite retrospective analysis of natural forest dieback for the Béni Mellal-Khénifra region of Morocco. Working exclusively from open data – IFN2 polygons, harmonised Landsat and Sentinel-2 archives, and the TerraClimate and ERA5-Land reanalyses – and from a reproducible Python pipeline, we quantify a cumulated dieback signal of approximately 187,700 ha (20.1%) of the 936,437 ha of natural forest over the 1984-2024 window. The BFAST retro-analysis identifies a measurable, species-differentiated signal across all six IFN2 strata: *Quercus suber* leads with 41.4% of pure stands showing dieback, *Cedrus atlantica* shows an intermediate rate (16.6% pure, 22.9% mixed), and *Quercus rotundifolia* shows the lowest per-stratum rate (11.0–18.8%) but the largest absolute affected area (142,591 ha) because of its dominant surface. Autocorrelation-corrected cross-correlations identify SPEI-12 as the strongest hydro-climatic correlate for both oak species ($r = +0.36$ for cork oak at lag 0; $r = +0.31$ for holm oak at lag 1) and indicate a balanced short-and-long-scale profile for Atlas cedar, while vapour-pressure-deficit anomaly covaries with NDVI at lag 0 for every species – a pattern consistent with stomatal-hydraulic regulation. The elevation-correlation gradient (Qs 991 m > Qr 1.362 m > Ca 1.908 m) inversely tracks SPEI-12 sensitivity, in broad agreement with biome-level patterns reported by Vicente-Serrano et al., (2013). Sentinel-2 detects substantially more dieback than Landsat for Atlas cedar (+18.3 to +26.3 percentage points), a difference compatible with the reduced pixel-crown size mismatch when the sensor footprint approaches the crown size of a mature *C. atlantica*, whereas Landsat retains value for cork oak thanks to its longer pre-disturbance baseline; the two archives are therefore complementary, and their joint use is likely to strengthen future operational monitoring.

Beyond the specific results, the analysis produces three operational outputs on which subsequent doctoral work can build: a georeferenced list of DBSCAN-identified hotspot centroids per species, dated by median first permanent-break year; a reproducible parquet layer of per-pixel dieback flags, ready for pairing with future field validation; and a publication-ready set of figures documenting the entire chain from location to species × climate lag structure. Two methodological caveats warrant emphasis. The SPEI reference window (1958–2000) is now exceeded by the ongoing 2019–2024 drought event, so SPEI-12 saturates at its parameterised floor over 4–18% of recent months; correlation values reported here may therefore underestimate the actual species-level sensitivity. Additionally, the recent-decline flag rescues signals that STL/PELT miss near the right-hand series edge, but its final classification (permanent versus transitory) will only crystallise after the 2025–2027 growing seasons; an updated analysis in three years, using pixel-complete rather than random-sample Landsat processing and paired with the concurrent field diagnostic of the subsequent doctoral paper, is therefore the natural follow-up. More broadly, the pipeline demonstrated here — twelve Python scripts, under 2,500 lines of code, execution time below six minutes on a consumer laptop — appears transferable to other Maghreb or Sahel regions for which IFN polygons and Landsat/Sentinel time series exist. The scientific stakes for these regions are considerable: North African forests occupy the southern warm edge of the Mediterranean biome and are among the most exposed to 21st-century drought (Cramer et al., 2018), and making their dieback trajectories legible at regional scale, on open data and reproducible pipelines, is an important step towards evidence-based adaptation policy.

Data availability statement

All satellite and climate data used in this study are freely available through Google Earth Engine (Gorelick et al., 2017) and the respective providers listed in Table 1. The IFN2 shapefile is not freely available on-line and was obtained through the regional forestry service (DRANEF Béni Mellal-Khénifra) under a memorandum of understanding attached to the doctoral program; The complete Python pipeline (twelve scripts, approximately 2,400 lines of code), all intermediate parquet files, and all diagnostic reports are archived at [https://doi.org/10.5281/zenodo.21358367] and are reproducible on a modern consumer laptop.

Acknowledgements

The authors gratefully acknowledge the National Agency of Waters and Forests for granting access to the Second National Forest Inventory (IFN2) shapefile. We thank the USGS/NASA Landsat programme, the ESA Copernicus Sentinel-2 mission, the TerraClimate and ERA5-Land

teams, and the Google Earth Engine platform for maintaining the open data infrastructure on which this analysis rests.

REFERENCES

1. Abatzoglou, J. T., Dobrowski, S. Z., Parks, S. A., Hegewisch, K. C. (2018). TerraClimate, a high-resolution global dataset of monthly climate and climatic water balance from 1958–2015. *Scientific Data*, *5*(1), 170191. https://doi.org/10.1038/sdata.2017.191
2. Alba-Sánchez, F., Abel-Schaad, D., López-Sáez, J. A., Romera-Romera, D., Pérez-Díaz, S., González-Hernández, A. (2025). Seven Millennia of *Cedrus atlantica* Forest Dynamics in the Western Rif Mountains (Morocco). *Forests*, *16*(9), 1441. https://doi.org/10.3390/f16091441
3. Allen, C. D., Macalady, A. K., Chenchouni, H., Bachelet, D., McDowell, N., Vennetier, M., Kitzberger, T., Rigling, A., Breshears, D. D., Hogg, E. H. (Ted), Gonzalez, P., Fensham, R., Zhang, Z., Castro, J., Demidova, N., Lim, J.-H., Allard, G., Running, S. W., Semerci, A., Cobb, N. (2010). A global overview of drought and heat-induced tree mortality reveals emerging climate change risks for forests. *Forest Ecology and Management*, *259*(4), 660–684. https://doi.org/10.1016/j.foreco.2009.09.001
4. Anderegg, W. R. L., Martinez-Vilalta, J., Cailleret, M., Camarero, J. J., Ewers, B. E., Galbraith, D., Gessler, A., Grote, R., Huang, C., Levick, S. R., Powell, T. L., Rowland, L., Sánchez-Salguero, R., Trotsiuk, V. (2016). When a tree dies in the forest: Scaling climate-driven tree mortality to ecosystem water and carbon fluxes. *Ecosystems*, *19*(6), 1133–1147. https://doi.org/10.1007/s10021-016-9982-1
5. Anderegg, W. R. L., Trugman, A. T., Badgley, G., Anderson, C. M., Bartuska, A., Ciais, P., Cullenward, D., Field, C. B., Freeman, J., Goetz, S. J., Hicke, J. A., Huntzinger, D., Jackson, R. B., Nickerson, J., Pacala, S., Randerson, J. T. (2020). Climate-driven risks to the climate mitigation potential of forests. *Science*, *368*(6497), eaaz7005. https://doi.org/10.1126/science.aaz7005
6. Beguería, S., Vicente-Serrano, S. M., Reig, F., Latorre, B. (2014). Standardized precipitation evapotranspiration index (SPEI) revisited: Parameter fitting, evapotranspiration models, tools, datasets and drought monitoring. *International Journal of Climatology*, *34*(10), 3001–3023. https://doi.org/10.1002/joc.3887
7. Borghetti, M., Castellaneta, M., Leonardi, S. (2026). Functional mechanisms and drought responses in Mediterranean oaks: Three decades of research and a categorical synthesis. *Trees*, *40*(4), 93. https://doi.org/10.1007/s00468-026-02794-3
8. Bretherton, C. S., Widmann, M., Dymnikov, V. P., Wallace, J. M., Bladé, I. (1999). The effective number of spatial degrees of freedom of a time-varying field. *Journal of Climate*, *12*(7), 1990–2009. https://doi.org/10.1175/1520-0442(1999)012%3C1990:TENOSD%3E2.0.CO;2
9. Camarero, J. J., Gazol, A., Sangüesa-Barreda, G., Oliva, J., Vicente-Serrano, S. M. (2015). To die or not to die: Early warnings of tree dieback in response to a severe drought. *Journal of Ecology*, *103*(1), 44–57. https://doi.org/10.1111/1365-2745.12295
10. Cheddadi, R., Henrot, A.-J., François, L., Boyer, F., Bush, M., Carré, M., Coissac, E., De Oliveira, P. E., Ficetola, F., Hambuckers, A., Huang, K., Lézine, A.-M., Nourelbait, M., Rhoujjati, A., Taberlet, P., Sarmiento, F., Abel-Schaad, D., Alba-Sánchez, F., Zheng, Z. (2017). Microrefugia, climate change, and conservation of *Cedrus atlantica* in the Rif Mountains, Morocco. *Frontiers in Ecology and Evolution*, *5*, 114. https://doi.org/10.3389/fevo.2017.00114
11. Cheesman, A. W., Cernusak, L. A. (2026). Susceptibility of tropical trees to drought: Context across scales. *Plant Biology*, *28*(3), 553–560. https://doi.org/10.1111/plb.70156
12. Choat, B., Jansen, S., Brodribb, T. J., Cochard, H., Delzon, S., Bhaskar, R., Bucci, S. J., Feild, T. S., Gleason, S. M., Hacke, U. G., Jacobsen, A. L., Lens, F., Maherali, H., Martínez-Vilalta, J., Mayr, S., Mencuccini, M., Mitchell, P. J., Nardini, A., Pittermann, J., … Zanne, A. E. (2012). Global convergence in the vulnerability of forests to drought. *Nature*, *491*(7426), 752–755. https://doi.org/10.1038/nature11688
13. Cleveland, R. B. (1990). *STL: A Seasonal-Trend Decomposition Procedure Based on Loess*. https://api.semanticscholar.org/CorpusID:64570714
14. Congalton, R. G., Green, K. (2019). *Assessing the Accuracy of Remotely Sensed Data: Principles and Practices, Third Edition* (3rd ed.). CRC Press. https://doi.org/10.1201/9780429052729
15. Cramer, W., Guiot, J., Fader, M., Garrabou, J., Gattuso, J.-P., Iglesias, A., Lange, M. A., Lionello, P., Llasat, M. C., Paz, S., Peñuelas, J., Snoussi, M., Toreti, A., Tsimplis, M. N., Xoplaki, E. (2018). Climate change and interconnected risks to sustainable development in the Mediterranean. *Nature Climate Change*, *8*(11), 972–980. https://doi.org/10.1038/s41558-018-0299-2
16. David, T. S., Henriques, M. O., Kurz-Besson, C., Nunes, J., Valente, F., Vaz, M., Pereira, J. S., Siegwolf, R., Chaves, M. M., Gazarini, L. C., David, J. S. (2007). Water-use strategies in two co-occurring Mediterranean evergreen oaks: Surviving the summer drought. *Tree Physiology*, *27*(6), 793–803. https://doi.org/10.1093/treephys/27.6.793

17. Driouech, F., Stafi, H., Khouakhi, A., Moutia, S., Badi, W., ElRhaz, K., Chehbouni, A. (2021). Recent observed country-wide climate trends in Morocco. *International Journal of Climatology*, *41*(S1). https://doi.org/10.1002/joc.6734
18. Ebisuzaki, W. (1997). A method to estimate the statistical significance of a correlation when the data are serially correlated. *Journal of Climate*, *10*(9), 2147–2153. https://doi.org/10.1175/1520-0442(1997)010%3C2147:AMTETS%3E2.0.CO;2
19. Elair, C., Rkha Chaham, K., Hadri, A. (2023). Assessment of drought variability in the Marrakech-Safi region (Morocco) at different time scales using GIS and remote sensing. *Water Supply*, *23*(11), 4592–4624. https://doi.org/10.2166/ws.2023.283
20. Ester, M., Kriegel, H.-P., Sander, J., Xu, X. (1996). A density-based algorithm for discovering clusters in large spatial databases with noise. *Proceedings of the Second International Conference on Knowledge Discovery and Data Mining, KDD'96*, 226–231.
21. Filahi, S., Tanarhte, M., Mouhir, L., El Morhit, M., Tramblay, Y. (2016). Trends in indices of daily temperature and precipitations extremes in Morocco. *Theoretical and Applied Climatology*, *124*(3–4), 959–972. https://doi.org/10.1007/s00704-015-1472-4
22. Filahi, S., Tramblay, Y., Mouhir, L., Diaconescu, E. P. (2017). Projected changes in temperature and precipitation indices in Morocco from high-resolution regional climate models. *International Journal of Climatology*, *37*(14), 4846–4863. https://doi.org/10.1002/joc.5127
23. Ghaffariyan, M. R. (2025). Silvopastoral systems as a strategy for drought resilience: A short international review. *Silva Balcanica*, *26*(1), 33–41. https://doi.org/10.3897/silvabalcanica.26.e127074
24. Gorelick, N., Hancher, M., Dixon, M., Ilyushchenko, S., Thau, D., Moore, R. (2017). Google Earth Engine: Planetary-scale geospatial analysis for everyone. *Remote Sensing of Environment*, *202*, 18–27. https://doi.org/10.1016/j.rse.2017.06.031
25. Hammoudy, W., Ilmen, R., Sinan, M. (2024). Projected changes of thermal, rainfall and drought indices in Morocco from high resolution climate models. *IOP Conference Series: Earth and Environmental Science*, *1398*(1), 012019. https://doi.org/10.1088/1755-1315/1398/1/012019
26. Harris, C. R., Millman, K. J., Van Der Walt, S. J., Gommers, R., Virtanen, P., Cournapeau, D., Wieser, E., Taylor, J., Berg, S., Smith, N. J., Kern, R., Picus, M., Hoyer, S., Van Kerkwijk, M. H., Brett, M., Haldane, A., Del Río, J. F., Wiebe, M., Peterson, P., … Oliphant, T. E. (2020). Array programming with NumPy. *Nature*, *585*(7825), 357–362. https://doi.org/10.1038/s41586-020-2649-2
27. Henchiri, M., Igbawua, T., Javed, T., Bai, Y., Zhang, S., Essifi, B., Ujoh, F., Zhang, J. (2021). Meteorological drought analysis and return periods over North and West Africa and Linkage with El Niño–Southern Oscillation (ENSO). *Remote Sensing*, *13*(23), 4730. https://doi.org/10.3390/rs13234730
28. Hosking, J. R. M. (1990). L-Moments: Analysis and estimation of distributions using linear combinations of order statistics. *Journal of the Royal Statistical Society Series B: Statistical Methodology*, *52*(1), 105–124. https://doi.org/10.1111/j.2517-6161.1990.tb01775.x
29. International Tree Mortality Network. (2025). Towards a global understanding of tree mortality. *New Phytologist*, *245*(6), 2377–2392. https://doi.org/10.1111/nph.20407
30. Killick, R., Fearnhead, P., Eckley, I. A. (2012). Optimal detection of changepoints with a linear computational cost. *Journal of the American Statistical Association*, *107*(500), 1590–1598. https://doi.org/10.1080/01621459.2012.737745
31. Knostmann, P., Rasoamanana, A., Krott, M. (2025). Beyond Morocco's green success story: Analysing actor-interests and deforestation under the "Strategy 2020–2030 forests of Morocco." *Forests Monitor*, *2*(1), 209–253. https://doi.org/10.62320/fm.v2i1.27
32. Li, X., Wu, T., Xia, K., Tang, H., Wang, X., Wang, S., Lyne, V., Zu, Y. (2026). Forest loss intensifies meteorological drought in more than half of Earth's climate zones. *Science Advances*, *12*(2), eadv7998. https://doi.org/10.1126/sciadv.adv7998
33. Linares, J. C., Taïqui, L., Camarero, J. J. (2011). Increasing drought sensitivity and decline of Atlas Cedar (*Cedrus atlantica*) in the Moroccan Middle Atlas Forests. *Forests*, *2*(3), 777–796. https://doi.org/10.3390/f2030777
34. Morales, A., López-Bernal, Á., Testi, L., Villalobos, F. J. (2021). Transpiration and photosynthesis of holm oak trees in southern Spain. *Trees, Forests and People*, *5*, 100115. https://doi.org/10.1016/j.tfp.2021.100115
35. Muñoz-Sabater, J. (2019). ERA5-Land hourly data from 1981 to present [dataset]. In *Copernicus Climate Change Service (C3S) Climate Data Store (CDS)*. https://doi.org/10.5194/essd-13-4349-2021
36. Navarro-Cerrillo, R. M., Manzanedo, R. D., Bohorque, J., Sánchez, R., Sánchez, J., Miguel, S. D., Solano, D., Qarro, M., Griffith, D., Palacios, G. (2013). Structure and spatio-temporal dynamics of cedar forests along a management gradient in the Middle Atlas, Morocco. *Forest Ecology and Management*, *289*, 341–353. https://doi.org/10.1016/j.foreco.2012.10.011
37. Pan, Y., Birdsey, R. A., Fang, J., Houghton, R., Kauppi, P. E., Kurz, W. A., Phillips, O. L., Shvidenko, A., Lewis, S. L., Canadell, J. G., Ciais, P., Jackson, R. B., Pacala, S. W., McGuire, A. D.,

Piao, S., Rautiainen, A., Sitch, S., Hayes, D. (2011). A large and persistent carbon sink in the world's forests. *Science*, *333*(6045), 988–993. https://doi.org/10.1126/science.1201609

38. Peguero-Pina, J. J., Vilagrosa, A., Alonso-Forn, D., Ferrio, J. P., Sancho-Knapik, D., Gil-Pelegrín, E. (2020). Living in drylands: Functional adaptations of trees and shrubs to cope with high temperatures and water scarcity. *Forests*, *11*(10), 1028. https://doi.org/10.3390/f11101028
39. Pyarali, K., Zhang, L., Liu, N., Al-Qubati, A., Sun, G. (2026). Quantifying the response of water and carbon balances to land cover and climate extremes across Germany. *Hydrology and Earth System Sciences*, *30*(13), 4157–4174. https://doi.org/10.5194/hess-30-4157-2026
40. Pyper, B. J., Peterman, R. M. (1998). Comparison of methods to account for autocorrelation in correlation analyses of fish data. *Canadian Journal of Fisheries and Aquatic Sciences*, *55*(9), 2127–2140. https://doi.org/10.1139/f98-104
41. Roy, D. P., Kovalskyy, V., Zhang, H. K., Vermote, E. F., Yan, L., Kumar, S. S., Egorov, A. (2016). Characterization of Landsat-7 to Landsat-8 reflective wavelength and normalized difference vegetation index continuity. *Remote Sensing of Environment*, *185*, 57–70. https://doi.org/10.1016/j.rse.2015.12.024
42. Samih, A., Petit, D., Maatouf, N., Trócoli, S., Habbaz, H., Rohi, L. (2024). Diversity of beetle communities in cork oak forest of Larache from Morocco. *Indian Journal of Entomology*, 1–12. https://doi.org/10.55446/IJE.2024.2590
43. Schneider, D. P., Deser, C., Fasullo, J., Trenberth, K. E. (2013). Climate data guide spurs discovery and understanding. *Eos, Transactions American Geophysical Union*, *94*(13), 121–122. https://doi.org/10.1002/2013EO130001
44. Serbouti, S., Ettaqy, A., Boukcim, H., Mdersa, M. E., El Ghachtouli, N., Abbas, Y. (2023). Forests and woodlands in Morocco: Review of historical evolution, services, priorities for conservation measures and future research. *International Forestry Review*, *25*(1), 121–145. https://doi.org/10.1505/146554823836838745
45. Sousa, V., Ferreira, J. P. A., Miranda, I., Quilhó, T., Pereira, H. (2021). *Quercus rotundifolia* Bark as a source of polar extracts: Structural and chemical characterization. *Forests*, *12*(9), 1160. https://doi.org/10.3390/f12091160
46. Terrab, A., Hampe, A., Lepais, O., Talavera, S., Vela, E., Stuessy, T. F. (2008). Phylogeography of North African Atlas cedar (*Cedrus atlantica*, Pinaceae): Combined molecular and fossil data reveal a complex Quaternary history. *American Journal of Botany*, *95*(10), 1262–1269. https://doi.org/10.3732/ajb.0800010
47. Truong, C., Oudre, L., Vayatis, N. (2020). Selective review of offline change point detection methods. *Signal Processing*, *167*, 107299. https://doi.org/10.1016/j.sigpro.2019.107299
48. Verbesselt, J., Hyndman, R., Newnham, G., Culvenor, D. (2010). Detecting trend and seasonal changes in satellite image time series. *Remote Sensing of Environment*, *114*(1), 106–115. https://doi.org/10.1016/j.rse.2009.08.014
49. Verbesselt, J., Zeileis, A., Herold, M. (2012). Near real-time disturbance detection using satellite image time series. *Remote Sensing of Environment*, *123*, 98–108. https://doi.org/10.1016/j.rse.2012.02.022
50. Vicente-Serrano, S. M., Beguería, S., López-Moreno, J. I. (2010). A Multiscalar drought index sensitive to global warming: The standardized precipitation evapotranspiration index. *Journal of Climate*, *23*(7), 1696–1718. https://doi.org/10.1175/2009JCLI2909.1
51. Vicente-Serrano, S. M., Gouveia, C., Camarero, J. J., Beguería, S., Trigo, R., López-Moreno, J. I., Azorín-Molina, C., Pasho, E., Lorenzo-Lacruz, J., Revuelto, J., Morán-Tejeda, E., Sanchez-Lorenzo, A. (2013). Response of vegetation to drought time-scales across global land biomes. *Proceedings of the National Academy of Sciences*, *110*(1), 52–57. https://doi.org/10.1073/pnas.1207068110
52. Vila-Viçosa, C., Almeida, R. (2020). Vila-Viçosa, C & Almeida, R. (2020) Lectotypification of names of *Quercus* spp. (Fagaceae) described by Lamarck from the Iberian Peninsula. Phytotaxa 455 (3): 205–213. *Phytotaxa*, *458*(2). https://doi.org/10.11646/phytotaxa.458.2.6
53. Virtanen, P., Gommers, R., Oliphant, T. E., Haberland, M., Reddy, T., Cournapeau, D., Burovski, E., Peterson, P., Weckesser, W., Bright, J., Van Der Walt, S. J., Brett, M., Wilson, J., Millman, K. J., Mayorov, N., Nelson, A. R. J., Jones, E., Kern, R., Larson, E., … Vázquez-Baeza, Y. (2020). SciPy 1.0: Fundamental algorithms for scientific computing in Python. *Nature Methods*, *17*(3), 261–272. https://doi.org/10.1038/s41592-019-0686-2
54. Zanaga, D., Van De Kerchove, R., De Keersmaecker, W., Souverijns, N., Brockmann, C., Quast, R., Wevers, J., Grosu, A., Paccini, A., Vergnaud, S., Cartus, O., Santoro, M., Fritz, S., Georgieva, I., Lesiv, M., Carter, S., Herold, M., Li, L., Tsendbazar, N.-E., … Arino, O. (2021). *ESA WorldCover 10 m 2020 v100* (Version v100) [Dataset]. Zenodo. https://doi.org/10.5281/ZENODO.5571936